Ceramics International xxx (xxxx) xxx

Contents lists available at ScienceDirect

Ceramics International

journal homepage: www.elsevier.com/locate/ceramint

Converting commercial Fe_2O_3 to effective anode material using glucose as "etching" agent

Chenxu Wang, Pedaballi Sireesha, Jing Shang, John S. McCloy, Jin Liu *, Wei-Hong Zhong **

School of Mechanical and Materials Engineering, Washington State University, Pullman, WA, 99164, USA

ARTICLE INFO

Handling Editor: Dr P. Vincenzini

Keywords:
Iron oxide
Nanostructure
Core-shell
Anode
Li-ion battery

ABSTRACT

Fe_2O_3 is an appealing anode material due to its high specific capacity (1007 mAh g^{-1}), low cost, natural abundance, and nontoxicity. However, its unstable structure during cycling processes has hindered its potential. In this study, we present a "green" synthesis method to fabricate stable porous Fe_2O_3 encapsulated in a buffering hollow structure (p-Fe_2O_3@h-TiO_2) as an effective anode material for Li-ion batteries. The synthesis process only involves glucose as an "etching" agent, without the need for organic solvents or difficult-to-control environments. Characterizations of the nanostructures, chemical compositions, crystallizations, and thermal behaviors for the intermediate/final products confirm the formation of p-Fe_2O_3@h-TiO_2. The synthesized Fe_2O_3 anode material effectively accommodates volume change, decreases pulverization, and alleviates agglomeration, leading to a high capacity that is over eleven times greater than that of the as-received commercial Fe_2O_3 after a long cycling process. This work provides an attractive, "green" and efficient method to convert commercially abundant resources like Fe_2O_3 into effective electrode materials for energy storage systems.

1. Introduction

Commercial lithium-ion batteries (LIBs) using conventional graphite anodes have been mass-produced to meet the expanding market of portable electronics and electronic vehicles because of their cycling stability and long lifespan [1]. However, graphite has a low theoretical capacity of 372 mA h g^{-1}, limiting the improvement of the energy density of LIBs. Therefore, many alternative anode materials with high theoretical specific capacities have been explored [2]. Transitional metal oxides, such as Fe_2O_3, Fe_3O_4, FeO, NiO, and MnO, have received extensive attention owing to their high theoretical capacity and environment-friendly properties [3–8]. Among them, Fe_2O_3 has been considered to be one of the most attractive anode candidates for LIBs because of the extra advantages of cost-effectiveness and natural abundance, in addition to the high theoretical capacity (1007 mAh g^{-1}). Despite these advantages, Fe_2O_3 suffers from large volume change, pulverization and severe agglomeration in the conversion reaction ($Fe_2O_3 + 6Li^+ + 6e^- \leftrightarrow 2Fe + 3Li_2O$) during the cycling process, leading to low Coulombic efficiency and rapid capacity decay [9].

To address the above-mentioned issues, many synthesis methods, such as coprecipitation [10,11], solvothermal [12], etching [13], and sol-gel, have been studied to fabricate various nanostructures for Fe_2O_3 anode (see Table S1). The coprecipitation methods were considered preferable synthetic methods to form nano-Fe_2O_3 because of their resulting facile size-controllable nanostructures obtainable (e.g., nanorod, nanocube, and nanoflower, etc.) and low-cost processing. For example, Fe_2O_3 nanorods were fabricated by using a simple heating process of ferric chloride aqueous solution with ammonia as the size-modifying agent. In spite of the cost-effectiveness, the reported research suggested that these Fe_2O_3 nanorods displayed poor capacity retention after long cycling processes, as a result of low porosity and agglomeration, which induced low ionic/electronic conductivities [10]. In contrast, the solvothermal methods using organic solvents were applied to fabricate nano-Fe_2O_3 with mesoporous structures (e.g., porous sphere, spindle, etc) and high specific surface area, which led to good cycling performances in LIBs. For instance, mesoporous Fe_2O_3 sunflower-like spheres were synthesized by solvothermal synthesis using ferric nitrate in N,N-dimethylformamide (DMF) as an organic solvent medium [12]. However, the products of solvothermal methods were low-yield; the use of large amounts of organic solvents increases the cost and causes environmental pollution. Similarly, sol-gel methods were also concerned for a high fabrication cost because of the low-yield and

* Corresponding author.
** Corresponding author.
E-mail addresses: jin.liu2@wsu.edu (J. Liu), katie_zhong@wsu.edu (W.-H. Zhong).

https://doi.org/10.1016/j.ceramint.2023.07.234
Received 11 May 2023; Received in revised form 2 July 2023; Accepted 25 July 2023
Available online 26 July 2023

large organic chemical consumption. Acids were needed to etch Fe_2O_3 particles for generating porous structures such as spheres and nanodiscs [14,15]. For instance, the Fe_2O_3 nanodiscs were etched by a high concentration (0.5 M) of oxalic acid to tune the porosity. Other acids such as hydrochloric acid and phosphoric acid were also used as the etching agents, but the use of acids increases the cost and causes new environmental issues [16,17]. Therefore, viable, "green" fabrication processes for the synthesis of desired Fe_2O_3 nanostructures have not been realized to obtain Fe_2O_3 anodes with high performance and low cost.

Numerous Fe_2O_3 composites, such as Fe_2O_3/C, Fe_2O_3/metal oxides and Fe_2O_3/MXenes, were synthesized through the methods mentioned above for enhancing the electrochemical performance of Fe_2O_3 anodes. One of the most reported nanostructures is the composites of Fe_2O_3/C, such as Fe_2O_3@C nanoparticles and nano-Fe_2O_3 incorporated carbon matrices. In such composites, carbon materials have been used to buffer the volume change, decrease the pulverization and mitigate the agglomeration of Fe_2O_3 [18]. For example, a Fe_2O_3@C composite with a carbon content of 50 wt% and a polypyrrole coating, stabilized the structure and enhanced the electronic conductivity of Fe_2O_3 [19]. However, introduction of the large amount of carbon decreases the content of active materials in electrodes, leading to a low energy density of the entire electrode. Therefore, many inorganic compounds such as TiO_2, SnO_2, and MnO_2 have been used as a thin coating for Fe_2O_3 nanoparticles to stabilize the structures [20]. For instance, TiO_2-coated Fe_2O_3 [21] and Fe_2O_3@SnO_2 nanorods [22] were reported to exhibit stable nanostructures and alleviated aggregation of Fe_2O_3. Among the inorganic coatings, TiO_2 possesses very stable nanostructures because of the extremely small volume change of 4% during lithiation/delithiation processes and fast lithium-ion diffusion [23]. Unfortunately, the essential non-elasticity of TiO_2 makes the TiO_2 surface coating hardly handle the volume change of active materials. Hence, hollow structures were reported as an efficient design for active materials to accommodate the large volume change. It is known that Si and SnO_2 also have large volume expansions of 400% and 260% during cycles. Si nanospheres [24] and SnO_2 nanowires [25] were encapsulated by a TiO_2 shell to form hollow structures to accommodate the volume expansion, exhibiting specific capacities five to ten times higher than that of untreated samples. Moreover, large volume-expansion active materials (including Fe_2O_3, Si and SnO_2, etc.) that were fabricated into porous structures demonstrated excellent electrochemical performance. The porous structures not only provided large electrode/electrolyte interfaces and facilitated ionic/electronic diffusion among active materials, but also decreased the structural strain during repeated lithiation/delithiation processes. Therefore, constructing a hollow structure with TiO_2 shell encapsulating porous Fe_2O_3 is potentially effective for accommodating the volume change and alleviating the pulverization/agglomeration of Fe_2O_3 during the cycling process, but complete studies of this have not been reported in the literature to date.

In the current study, we fabricate porous Fe_2O_3 using glucose as an "etching" agent, and then prepare a hollow structure with a TiO_2 shell encapsulating the porous Fe_2O_3 (*p*-Fe_2O_3@*h*-TiO_2, where "*p*" stands for "porous" and "*h*" for hollow) from commercial Fe_2O_3 particles (for cosmetic applications). This is a viable, "green" fabrication approach because the process only involves using glucose as the "etching" agent, and only simple heating processes under easily controllable environments are required, without using any organic solvents. Concentrations of raw materials are optimized to effectively form the desired hollow structures in high yields. The synthesis mechanism is analyzed through the characterizations of the nanostructure, chemical compositions, crystallization and thermal behavior of the intermediate, indicating the formation of *p*-Fe_2O_3@*h*-TiO_2 as the final synthesis product. This hollow structural anode material has been demonstrated to be able to buffer the volume change, alleviate the pulverization, and reduce the agglomeration of Fe_2O_3 particles. As the anode, the resulting anode material builds up a high specific capacity over eleven times higher than that of the as-received commercial Fe_2O_3 in LIBs. This work provides an attractive "green" and efficient fabrication method of converting commercial abundant resources such as Fe_2O_3 into effective electrode materials for energy storage systems.

2. Experiments

2.1. Raw materials

The Li metal circuit plates with a diameter of 15.8 mm were purchased from China Energy Lithium Co., Ltd. The carbon ester electrolyte purchased from Sigma-Aldrich Co., Ltd is composed of 1.0 M $LiPF_6$ in a mixed solvent of ethylene carbonate (EC) and ethyl methyl carbonate (EMC) (1:1 by volume). Fe_2O_3 powder was purchased from Thermo Scientific Co., Ltd. Titanium (IV) oxysulfate ($TiOSO_4$) and glucose were purchased from Sigma-Aldrich Co., Ltd. The separator (Celgard 2400) and electrode components including Cu foil, super C45 and polyvinylidene fluoride binder (PVDF) were purchased from MTI Co., LTD. N-methy-l-2-pyrrolidone (NMP) was purchased from Sigma-Aldrich Co., Ltd.

2.2. Preparation of Fe_2O_3@C

Fe_2O_3@C was synthesized by a hydrothermal process. Firstly, glucose solution (0.05 M) was prepared by dissolving 0.27 g glucose into 30 mL water. Then, 1 g commercial Fe_2O_3 was dispersed into the glucose solution by sonication for 5 min. The solution was transferred into 40 mL Teflon-lined stainless-steel autoclave, sealed and heated at 170 °C for 10 h in an air-blowing thermostatic oven. After cooling to ambient temperature, the precipitates were collected by filtration with a nylon filter film and washed with deionized water and ethanol for three times. Thereafter, the precipitates were dried in a vacuum oven at 60 °C for 10 h. Other combinations of glucose concentrations (0.5 and 0.1 M) and Fe_2O_3 amounts (0.1 and 0.5 g) were also used to synthesize samples during the optimization process of the synthesis design.

2.3. Preparation of Fe_2O_3@C@$TiO(OH)_2$

Fe_2O_3@C@$TiO(OH)_2$ was fabricated by a facile coating process. $TiOSO_4$ solution was first prepared by dissolving 0.05 g $TiOSO_4$ and 3 g H_2SO_4 solution (1 mol L^{-1}) in 100 mL deionized water. Note that the H_2SO_4 solution was added into the solution by drop by drop. Then, Fe_2O_3@C was dispersed in $TiOSO_4$ solution with sonication for 30 min and a continued magnetic stirring process for 5 h. After a filtration process with a nylon filter film, the precipitates were washed with deionized water and ethanol for three times and dried in a vacuum oven at 60 °C.

2.4. Preparation of *p*-Fe_2O_3@*h*-TiO_2

p-Fe_2O_3@*h*-TiO_2 was prepared by a calcination process. The as-prepared precursor, Fe_2O_3@C@$TiO(OH)_2$, was calcined at 500 °C in air atmosphere for 2 h. The heating rate of calcination process is 5 °C min^{-1}. Finally, *p*-Fe_2O_3@*h*-TiO_2 was obtained and collected for further characterization and battery assembly.

2.5. Materials characterization

The morphologies of Fe_2O_3@C and *p*-Fe_2O_3@*h*-TiO_2 were characterized by a scanning electron microscope (FE-SEM, S4800, Hitachi) and a transmission electron microscope (TEM, JEOL JEM-2100). The specific surface area and porosity were determined by a Micromeritics ASAP 2020Plus accelerated surface area and porosimetry system at 77 K; a degassing process under a vacuum of $\sim 10^{-6}$ bar was conducted at 150 °C for 12 h to activate the samples. The chemical composition and crystallization of the commercial Fe_2O_3, Fe_2O_3@C, Fe_2O_3@C@$TiO(OH)_2$ and *p*-Fe_2O_3@*h*-TiO_2 were investigated by Fourier transform

infrared spectroscopy-attenuated total reflectance (FTIR-ATR, Thermo fisher iS10), Raman spectroscopy (Thermofisher DXR2xi) and X-ray diffraction (XRD, Cu K_α, $\gamma = 1.54$ Å, Panalytical X'pert Pro). The scan step of FTIR is 0.5 cm^{-1}. The Raman laser excitation wavelength is 532 nm (4 cm^{-1} spectral resolution) and the laser power was set to 5.2 mW. The exposure time of Raman is 0.0833 s and averaged over 80 scans. The composition ratio of all samples was measured by thermogravimetric analysis (TGA, SDT Q600, Switzerland) to analyze the carbon content of the composites at a heating rate of 5 °C min^{-1} in air from room temperature to 600 °C. Differential scanning calorimetry (DSC, Mettler Toledo) was applied to test the thermal properties of the films with a heating rate of 5 °C min^{-1} in air.

2.6. Electrochemical measurements

To test the electrochemical performance, the 2025 coin-type cells were assembled. To fabricate the electrode sheet, a slurry was prepared by mixing the synthesized *p*-Fe_2O_3@*h*-TiO_2 powders with conductive agent (super C45), binder (PVDF) at a weight ratio of 8:1:1 in NMP solvent by magnetic stirrer for 10 h. Thereafter, the homogenous slurry was dried on copper sheet and was transferred into a vacuum oven for 12 h under 80 °C to further remove the remaining moisture. The obtained electrode sheet was cut into circular plates with a diameter of 12.7 mm, and the average area loading of active materials is ~2.8 mg cm^{-2}. A Li plate was applied as the counter electrode. When assembling coin cells, the electrolyte amount (40 μL) and assembly pressure (50 MPa) were controlled to keep them consistent for comparison. The cycling performance was tested by a LAND multichannel battery cycler (Wuhan LAND Electronics Co., Ltd.). The assembled half cells were cycled in a voltage range of 0.1–3 V (vs Li^+/Li) at various rates of 0.1 C, 0.2 C, 0.5 C, 0.8 C and 1 C. The electrochemical impedance spectroscopy (EIS) measurements were tested in a frequency range of 0.1–10^6 Hz on an electrochemical workstation (BioLogic VSP). Cyclic voltammetry (CV) experiments were also carried out by the electrochemical

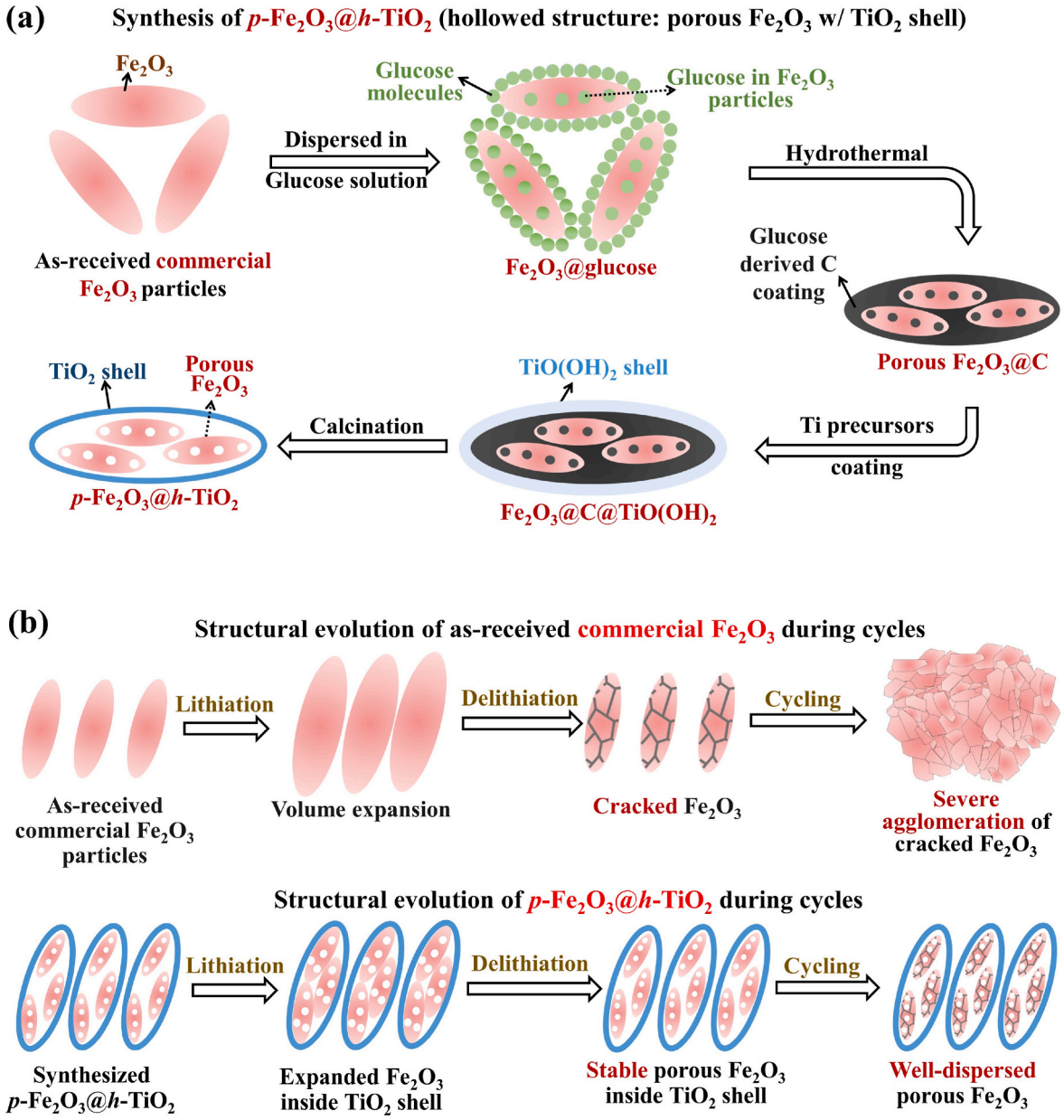

Fig. 1. (a) Synthesis processes of the hollow structure with a TiO_2 shell encapsulating porous Fe_2O_3 (*p*-Fe_2O_3@*h*-TiO_2). (b) The structure evolution of the commercial Fe_2O_3 and *p*-Fe_2O_3@*h*-TiO_2 during cycling processes when applied as the anode in Li-ion batteries.

workstation from 0 V to 3 V.

3. Results and discussions

3.1. Synthesis of p-Fe_2O_3@h-TiO_2

Fig. 1a presents the schematic of the glucose-assisted synthesis process of *p*-Fe_2O_3@*h*-TiO_2. As shown, within the glucose solution, the commercial Fe_2O_3 particles (Fig. S1a) adsorb glucose molecules on their surface to form a glucose coating (Fe_2O_3@glucose). Meanwhile, some glucose molecules permeate the defects of Fe_2O_3 particles. In the hydrothermal process under a temperature of 170 °C for 10 h, the glucose molecules "etch" the Fe_2O_3 particles into a porous structure [26,27]. At the same time, the coating is gradually carbonized into a carbon shell for Fe_2O_3 particles (Fe_2O_3@C). Progressively, the particles accumulate together to form larger Fe_2O_3@C particles containing a number of Fe_2O_3 particles. To prepare the TiO_2 shell, titanium oxysulfate ($TiOSO_4$) is dissolved in water to form $TiO(OH)_2$ colloids as the titanium precursor [28]. The pH of the $TiOSO_4$ solution is controlled by sulfuric acid to build a chemical equilibrium between $TiOSO_4$ (aq) and $TiO(OH)_2$ (sol). After dispersing Fe_2O_3@C particles into the $TiOSO_4$ solution, the carbon shell with rich O-containing functional groups adsorbs $TiO(OH)_2$ on the surface and generates a $TiO(OH)_2$ shell (Fe_2O_3@C@$TiO(OH)_2$) [23]. Then, the Fe_2O_3@C@$TiO(OH)_2$ powder is calcined at 500 °C for 2 h to remove carbon to generate the hollow structure with a TiO_2 shell encapsulating the porous Fe_2O_3 (*p*-Fe_2O_3@*h*-TiO_2).

3.2. Optimization of the synthesis process

To optimize the synthesis process, various concentrations of glucose and commercial Fe_2O_3 particles were applied during the hydrothermal process (Table S2). In 0.5 M glucose solution without the addition of Fe_2O_3 particles, the products of the hydrothermal process are carbon microspheres with diameters of 1.5–6 μm (Fig. S1b). These carbon spheres are formed through a homogeneous nucleation process. After adding 0.5 g Fe_2O_3 particles inside, many Fe_2O_3@C particles emerged among carbon microspheres in the hydrothermal process product (Fig. S1c). The diameter range of carbon spheres is 1–10 μm. This diameter-range change is ascribed to the heterogeneous nucleation of carbon spheres with Fe_2O_3 particles as nuclei. Hence, we proposed that glucose first forms a carbon coating and grows on Fe_2O_3 nuclei; and then, the excessive amount of glucose generates carbon microspheres. When the glucose concentration decreases to 0.1 M and Fe_2O_3 amount decreases to 0.1 g, both carbon spheres and Fe_2O_3@C particles appear in the hydrothermal product, indicating glucose amount is still in excess for the formation of Fe_2O_3@C (Fig. S1d). With a further increase of Fe_2O_3 amount to 0.5 g and keeping glucose concentration at 0.1 M, more Fe_2O_3@C particles and fewer carbon microspheres are present in the products (Fig. S1e). Hence, we optimize the glucose concentration to 0.05 M and Fe_2O_3 amount to 1 g. The optimized hydrothermal product only contains Fe_2O_3@C particles and no carbon microsphere included (Fig. S1f, 2a). In the below context, the samples for characterization refer to the products fabricated by the optimized synthesis process.

3.3. Structural evolution of p-Fe_2O_3@h-TiO_2 during cycling processes

The stable cycling structural mechanism of *p*-Fe_2O_3@*h*-TiO_2 is illustrated in Fig. 1b. During cycling processes in LIBs, the lithiation induces an expansion, while delithiation causes the shrinking of Fe_2O_3 particles, which leads to the cracking of particles because of the volume change. After many cycles, the Fe_2O_3 particles are severely agglomerated due to repeated severe volume changes and consequent pulverization of Fe_2O_3. Agglomeration of the Fe_2O_3 particles results in low ionic/electronic conductivities of the electrode, leading to a low specific capacity and short lifespan [29]. On the contrary, for *p*-Fe_2O_3@*h*-TiO_2, the expanded and cracked porous Fe_2O_3 particles are confined in the stable TiO_2 shell, which effectively prevents the severe agglomeration of Fe_2O_3. The good dispersion and porous structure of Fe_2O_3 inside the TiO_2 shell together lead to good ionic conductivity even after many expansion-shrinkage cycles, thus resulting in superior cycling performance.

3.4. Characterization of intermediate products and p-Fe_2O_3@h-TiO_2

The morphology of Fe_2O_3@C and *p*-Fe_2O_3@*h*-TiO_2 was investigated by scanning electron microscopy (SEM) and transmission electron microscope (TEM) to confirm the formation of *p*-Fe_2O_3@*h*-TiO_2 nanostructures. Fig. S1f, 2a depict the SEM images of Fe_2O_3@C, which indicates the nanoworm-like structure of Fe_2O_3@C. In addition, their measured average dimensional length and width are 215 nm and 108 nm, respectively. The Fe_2O_3@C composite structure is further confirmed by TEM images. As shown in Fig. 2b, S2a-c, the nanoworm-like amorphous carbon particles are incorporated with many porous Fe_2O_3 particles inside. The high-resolution transmission electron microscopy (HRTEM) images of Fe_2O_3@C reveal a lattice fringe value of 0.27 nm (Fig. S2d), which is approximate to the lattice fringe value of 0.25 nm for the (110) plane of α-Fe_2O_3 [30]. Meanwhile, abundant pores surrounded by Fe_2O_3 crystals can be found in Fig. 2c, demonstrating the porous structure of Fe_2O_3 particles. After titanium precursor coating, a very rough surface of the particles with adhered $TiO(OH)_2$ can be found in the SEM images of Fe_2O_3@C@$TiO(OH)_2$ (Fig. S3). Thereafter, followed by a calcination process, *p*-Fe_2O_3@*h*-TiO_2 particles with lengths of ~76.2 nm and widths of ~24.5 nm are obtained (Fig. 2d). The TEM images of *p*-Fe_2O_3@*h*-TiO_2 demonstrate its hollow nanostructure (Fig. 2e, S4a, S4b). Fig. 2f, S4c show the TiO_2 shell around Fe_2O_3 particles, confirming the structure of *p*-Fe_2O_3@*h*-TiO_2. In the HRTEM images (Fig. S4d), the lattice fringe of 0.351 nm is ascribed to the (101) plane of the anatase TiO_2 shell [31].

The pore size and specific surface area of the commercial Fe_2O_3 and *p*-Fe_2O_3@*h*-TiO_2 were examined by nitrogen adsorption/desorption isotherm analysis. As shown in Fig. S5, both samples show typical type-IV isotherm curves. The volumes of the pores with size range from 5 nm to 30 nm significantly increase (Insert of Fig. S5). This result demonstrates that more nanopores are present in p-Fe_2O_3@h-TiO_2 than that in the commercial Fe_2O_3. Moreover, *p*-Fe_2O_3@*h*-TiO_2 shows a larger specific surface area of 63.83 $m^2\ g^{-1}$ (vs. 50.13 $m^2\ g^{-1}$ of the commercial Fe_2O_3) because of the increased amount of nanopores.

The chemical compositions of *p*-Fe_2O_3@*h*-TiO_2 and its precursors were characterized by Fourier transform infrared spectroscopy (FTIR) to study the formation process (Fig. 2g). For the commercial Fe_2O_3, the broad peak at 3388 cm^{-1} is ascribed to the stretching vibration of O–H [32]. A weak peak at 2169 cm^{-1} can be attributed to the stretching of C═O═C. The presence of O–H and C═O═C is speculated due to the remaining functional groups on the surface of Fe_2O_3 particles. The typical peak of Fe–O stretching mode is found at 640 cm^{-1}. After the formation of a glucose-derived carbon shell in the hydrothermal process, an extra peak of O–H is found at 3504 cm^{-1} in the spectra of Fe_2O_3@C and Fe_2O_3@C@$TiO(OH)_2$. More peaks are present at 2641 cm^{-1}, 2315 cm^{-1}, 2070 cm^{-1},1733 cm^{-1}, and 744 cm^{-1}, which belong to the stretching or bending vibration of carbon-related bonds such as C–H, C═O, C═C and C–O, respectively [33]. These carbon-related bonds demonstrate diverse functional groups in the amorphous carbon of Fe_2O_3@C, thus, leading to good absorption of $TiO(OH)_2$ colloids on the surface. Meanwhile, there is no significant difference between Fe_2O_3@C and Fe_2O_3@C@$TiO(OH)_2$, indicating that the amorphous carbon of Fe_2O_3@C still keeps integrity and is not dissolved or dispersed into $TiOSO_4$ solutions during the sonication and mixing process. Regarding *p*-Fe_2O_3@*h*-TiO_2, a strong peak of OH appears at 2978 cm^{-1}, which is due to the surface functional groups on the TiO_2 shell. Notably, compared to the commercial Fe_2O_3, the Fe–O peak of *p*-Fe_2O_3@*h*-TiO_2 has a blue shift from 640 cm^{-1} to 628 cm^{-1}. This phenomenon is speculated induced by the impact of the hydrothermal and calcination

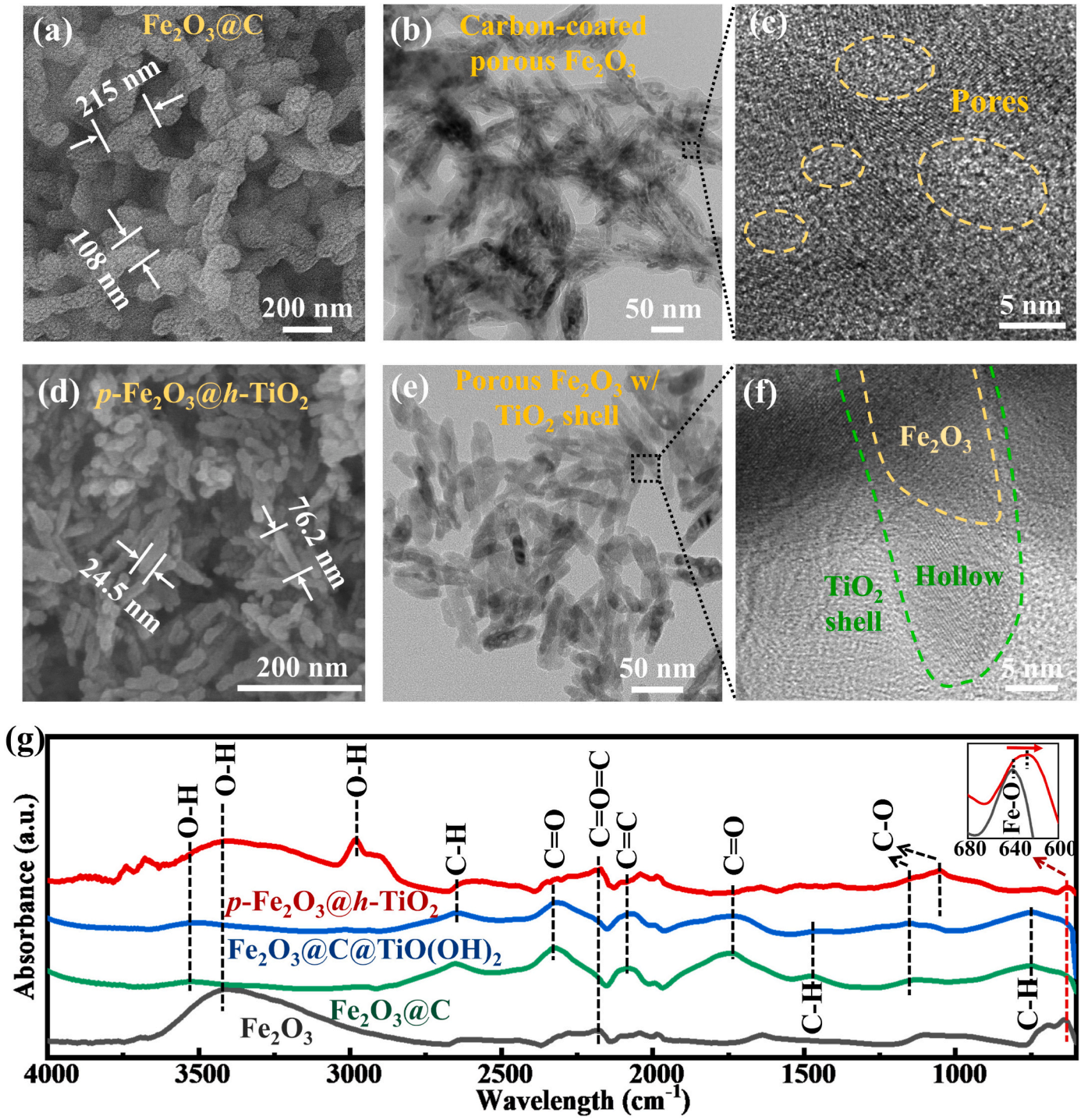

Fig. 2. Characterization of intermediate products and *p*-Fe_2O_3@*h*-TiO_2. SEM images of (a) Fe_2O_3@C and (d) *p*-Fe_2O_3@*h*-TiO_2. TEM images of (b) Fe_2O_3@C and (e) *p*-Fe_2O_3@*h*-TiO_2. HRTEM images of (c) Fe_2O_3@C and (f) *p*-Fe_2O_3@*h*-TiO_2; the inset images are the enlarged area of lattice fringes. (g) ATR-FTIR curves of Fe_2O_3, Fe_2O_3@C, Fe_2O_3@C@$TiO(OH)_2$ and *p*-Fe_2O_3@*h*-TiO_2.

process on the crystallization of Fe_2O_3 and the impact of TiO_2 peaks [34].

The crystal structures of various samples were revealed by X-ray diffraction (XRD). As shown in Fig. 3a, the typical peaks of both α-Fe_2O_3 and γ-Fe_2O_3 can be found in the curve of the commercial Fe_2O_3 [35]. The curves of Fe_2O_3@C and Fe_2O_3@C@$TiO(OH)_2$ do not show new peaks, demonstrating that the hydrothermal and Ti-precursor-coating processes have a small impact on the primary crystal structure of Fe_2O_3. After the calcination process, typical peaks of TiO_2 are found at 24.3°, 40.9° and 49.6°, which belong to the planes of (101), (111) and (200), respectively [36]. A strength-increased peak at 33.3°, which belongs to the (104) plane of α-Fe_2O_3 in *p*-Fe_2O_3@*h*-TiO_2, demonstrates the increased amount of α-Fe_2O_3 in the sample [12]. This result is due to the calcination process that transforms the crystal structure of Fe_2O_3 from γ-phase to α-phase [37]. Moreover, the peaks in the range of 42–80° of *p*-Fe_2O_3@*h*-TiO_2 display a right shift compared to the as-received commercial Fe_2O_3. This peak shift demonstrated the improved crystallization of *p*-Fe_2O_3@*h*-TiO_2 that enhances the stability of the Fe_2O_3 structure during the cycling process.

Fig. 3b illustrates the Raman spectra of various samples. Six typical

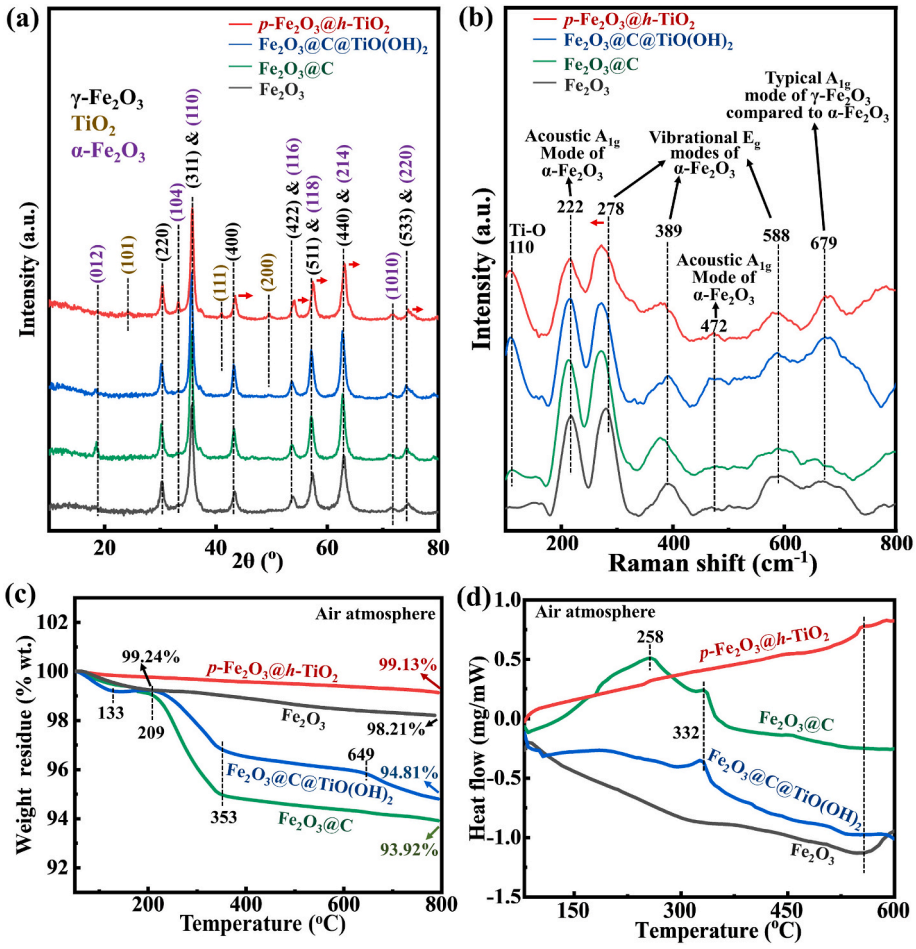

Fig. 3. (a) XRD, (b) Raman, (c) TGA and (d) DSC results of Fe_2O_3, Fe_2O_3@C, Fe_2O_3@C@TiO(OH)$_4$ and *p*-Fe_2O_3@*h*-TiO_2.

characteristic peaks of α-phase Fe_2O_3 were found in all the spectra. The peaks at 278 cm^{-1}, 389 cm^{-1} and 588 cm^{-1} are assigned to the vibrational E_g modes of α-Fe_2O_3. The peaks derived from the acoustic A_{1g} mode of α-Fe_2O_3 are located at 222 cm^{-1} and 472 cm^{-1}. A typical A_{1g} mode of γ-Fe_2O_3 can be found at 679 cm^{-1}, demonstrating the presence of γ-Fe_2O_3 in the samples [12,38]. Moreover, a shift of the peak at 278 cm^{-1} indicates the strain change and structural evolution during the hydrothermal and calcination processes of Fe_2O_3 [39]. In addition, a peak of E_g mode of TiO_2 presents at 110 cm^{-1} on spectra of Fe_2O_3@C@TiO(OH)$_2$ and *p*-Fe_2O_3@*h*-TiO_2, indicating that the TiO(OH)$_2$ are adsorbed on the surface of Fe_2O_3@C and the formation of TiO_2 shell with a hollow space [40].

Thermal gravimetric analysis (TGA) was performed for all the samples under an air atmosphere from 50 °C to 800 °C to study the composition evolution at different synthesis processes (Fig. 3c). For the commercial Fe_2O_3, the weight residue decreases to 99.24% in the first stage from 50 °C to 209 °C, which is due to the loss of –OH on the surface. Then the weight of the commercial Fe_2O_3 continues slowly decrease to 98.21% at 785.6 °C because of the loss of organic residues. In comparison, the curve of *p*-Fe_2O_3@*h*-TiO_2 has only one stage and the weight decreases to 99.13% at 793.2 °C. This weight loss (0.87%) is close to that (1.03%) of the phase transformation of the commercial Fe_2O_3. In sharp contrast, Fe_2O_3@C has three clear stages that are attributed to water removal (50–209 °C), decomposition of organic compositions (209–353 °C) and Fe_2O_3 phase transformation (353–800 °C) [41]. The weight loss of Fe_2O_3@C in the second stage is 4.07% which represents the carbon weight ratio in Fe_2O_3@C. For Fe_2O_3@C@TiO(OH)$_2$, the weight ratio of carbon is 2.47%, smaller than that of Fe_2O_3@C. This phenomenon may be due to the partial dispersion of amorphous carbon in $TiOSO_4$ solution. In specific, a peak at 649 °C on the curve of Fe_2O_3@C@TiO(OH)$_2$ could be caused by the Ti ion doping in surface Fe_2O_3. The small weight loss demonstrates the structure stability of *p*-Fe_2O_3@*h*-TiO_2 [42].

Differential scanning calorimetry (DSC) analysis was applied to further study the phase transformation of Fe_2O_3 and TiO_2 in various samples (Fig. 3d). The commercial Fe_2O_3 has an endothermic peak at 557 °C because of the phase transformation of Fe_2O_3 from γ-phase to α-phase. The peaks of Fe_2O_3@C and Fe_2O_3@C@TiO(OH)$_2$ at 332 °C are ascribed to the exothermic reaction of carbon. The smaller heat flow of Fe_2O_3@C@TiO(OH)$_2$ than that of Fe_2O_3@C can be assigned to the endothermic reaction of TiO(OH)$_2$ decomposition [43]. In contrast to the commercial Fe_2O_3, *p*-Fe_2O_3@*h*-TiO_2 does not show an obvious strong peak on the curve, further proving its stable structure.

3.5. *Electrochemical performance of p-Fe_2O_3@h-TiO_2*

In order to characterize the electrochemical performance of as-synthesized samples, half cells with the sample electrodes were prepared and a series of electrochemical measurements were performed. The impedances in Nyquist plots of the assembled half cells at different stand-still times are shown in Fig. 4a and b [44,45]. At the time after cell assembly with no standstill, charge transfer resistance (R_{ct}) of the cell with *p*-Fe_2O_3@*h*-TiO_2 electrode (124.4 Ω) is larger than that of the cell with Fe_2O_3 electrode (92.42 Ω) (Table S3). This result is due to the insufficient saturation and diffusion of liquid electrolytes in the hollow structure of *p*-Fe_2O_3@*h*-TiO_2 within a short standstill time. Thus, the resistance (R_{SEI}) of solid electrolyte interface (SEI) of the cell with *p*-Fe_2O_3@*h*-TiO_2 electrode (8.993 Ω) is smaller than that of the cell with

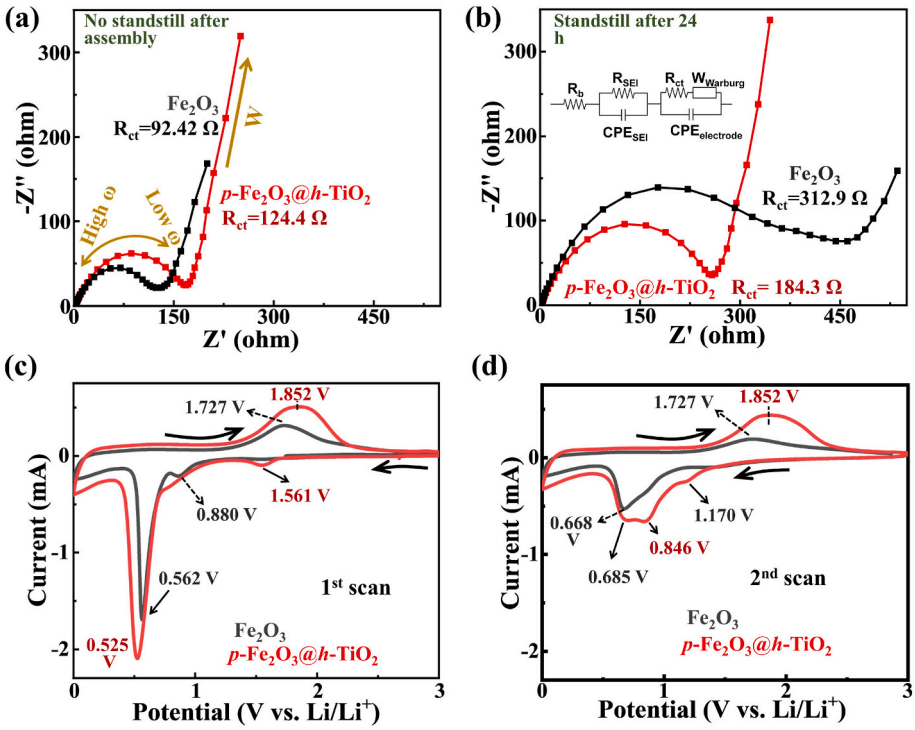

Fig. 4. Electrochemical characterization of Fe_2O_3 and *p*-Fe_2O_3@*h*-TiO_2 electrodes. EIS curves at (a) the initial state without standstill after assembly and (b) the stable state after the standstill for 24 h. (c) The 1st and (d) the 2nd cyclic voltammograms at a scan rate of 2 mV s^{-1}.

Fe_2O_3 electrode (3.784 Ω). After a standstill period of 24 h, SEI grows and the R_{SEI} increase to 22.47 Ω and 17.22 Ω for cell with *p*-Fe_2O_3@*h*-TiO_2 and Fe_2O_3 electrode, respectively. Meanwhile, the cell with *p*-Fe_2O_3@*h*-TiO_2 electrode shows a smaller R_{ct} (184.3 Ω) than the cell with Fe_2O_3 electrode (312.9 Ω), demonstrating that the liquid electrolyte has good contact with the porous Fe_2O_3 core and TiO_2 shell, and *p*-Fe_2O_3@*h*-TiO_2 enhances the ionic/electronic conductivities in electrodes.

Fig. 4c and d shows the first and second cyclic voltammograms (CV) curve of half cells with the commercial Fe_2O_3 and *p*-Fe_2O_3@*h*-TiO_2 electrodes. In Fig. 4c, the sharp cathodic peak of Fe_2O_3 at 0.562 V is attributed to the formation of SEI in the first cycle, while the peak shift to 0.525 V in the curve of *p*-Fe_2O_3@*h*-TiO_2, which is speculated as due to the partly phase change and increased crystallization of Fe_2O_3 during hydrothermal and calcination processes as demonstrated in previously [46]. The weak peak at 0.880 V is due to the phase transformation (hexagonal to cubic) of $Li_xFe_2O_3$ during delithiation process, while this peak is not found in *p*-Fe_2O_3@*h*-TiO_2, indicating the high stability of Fe_2O_3 crystal structure in *p*-Fe_2O_3@*h*-TiO_2. The peak at 1.561 V is the typical cathodic peak of TiO_2 in the first cycle, which shows that the TiO_2 shell of *p*-Fe_2O_3@*h*-TiO_2 also takes part in the cycling process of batteries [47]. The broad anodic peak at around 1.727 V for Fe_2O_3 is associated with the oxidation of Fe^0 to Fe^{2+}/Fe^{3+}. In comparison to Fe_2O_3, *p*-Fe_2O_3@*h*-TiO_2 has a broader anodic peak at 1.852 V, this shift of anodic peak may be due to the effect of the typical anodic peak of TiO_2 at 2.2 V and the increased crystallization of Fe_2O_3. In Fig. 4d, the cathodic peak of Fe_2O_3 in the second scan shifts to 0.668 V due to irreversible phase transformation compared to the first lithiation/delithiation processes [48]. A broad cathodic peak of *p*-Fe_2O_3@*h*-TiO_2 is presented in 0.685–0.846 V, which is due to the high participation of the Fe_2O_3 of *p*-Fe_2O_3@*h*-TiO_2 in lithiation/delithiation process compared to the commercial Fe_2O_3. The partial lithiation peak of Fe_2O_3 appears at 1.170 V in *p*-Fe_2O_3@*h*-TiO_2 while is not shown in the commercial Fe_2O_3. This phenomenon is induced by the high electrolyte contact area of porous Fe_2O_3 in *p*-Fe_2O_3@*h*-TiO_2 that facilitates the lithiation process of Fe_2O_3.

The discharge/charge profiles of the commercial Fe_2O_3 and *p*-Fe_2O_3@*h*-TiO_2 in the first, second and fourth cycles with a potential window from 0.1 V to 3 V are shown in Fig. 5a–c. For both samples, two plateaus at around 0.8 V and 1.7 V can be found in discharge and charge curves, respectively, which are attributed to the lithiation/delithiation processes of Fe_2O_3. At the first cycle of Fe_2O_3 electrode with a current density of 0.1 C (1 C = 1007 mA g^{-1}), a polarization at 1.3644 V of the charge curve and a small stage at 0.9522 V of the discharge curve can be found (Fig. 5a). This result indicates the sluggish Li ion diffusion of Fe_2O_3 electrode. The Fe_2O_3 delivers an initial discharge capacity of 1043.8 mAh g^{-1}. In comparison with the commercial Fe_2O_3, *p*-Fe_2O_3@*h*-TiO_2 exhibits a high discharge capacity of 1093.4 mAh g^{-1} at the first cycle. Notably, this value is larger than the first charge capacity of *p*-Fe_2O_3@*h*-TiO_2 (1006.2 mAh g^{-1}), which is likely due to the comparatively slower electrolyte saturation process of *p*-Fe_2O_3@*h*-TiO_2. Moreover, due to the unstable electrode structure of the commercial Fe_2O_3, some unstable voltage points can be found at the end of delithiation process of the commercial Fe_2O_3. At the second cycle under a current density of 0.1 C, the unstable voltage appears again at the end of delithiation process of the commercial Fe_2O_3, further demonstrating the pulverization and unstable electrode structure of Fe_2O_3 that are caused by its volume expansion during cycles (Fig. 5b). The discharge capacity of the commercial Fe_2O_3 and *p*-Fe_2O_3@*h*-TiO_2 at the second cycle are 626.8 mAh g^{-1} and 882.7 mAh g^{-1}, respectively. It is worthy note that the charge capacity of the first and second cycles are significantly larger than the discharge capacity. This phenomenon is because of new SEI formation on the surface of Fe_2O_3 particles in initial several cycles. Meanwhile, the Fe_2O_3 particles crack easily due to the unstable Fe_2O_3 structure, leading to exposure of more fresh surfaces, responsible for further inducing formation of SEI and more charge consumption [49]. Under a current density of 0.2 C at the fourth cycle, the electrode structure of Fe_2O_3 becomes stable but the discharge capacity decreases to 482.7 mAh g^{-1} because of the severe agglomeration of Fe_2O_3 compared to *p*-Fe_2O_3@*h*-TiO_2 (893.3 mAh g^{-1}) (Fig. 5c).

The rate performance of the commercial Fe_2O_3 and *p*-Fe_2O_3@*h*-TiO_2 electrodes was tested at various current densities from 0.1 C to 2 C. As

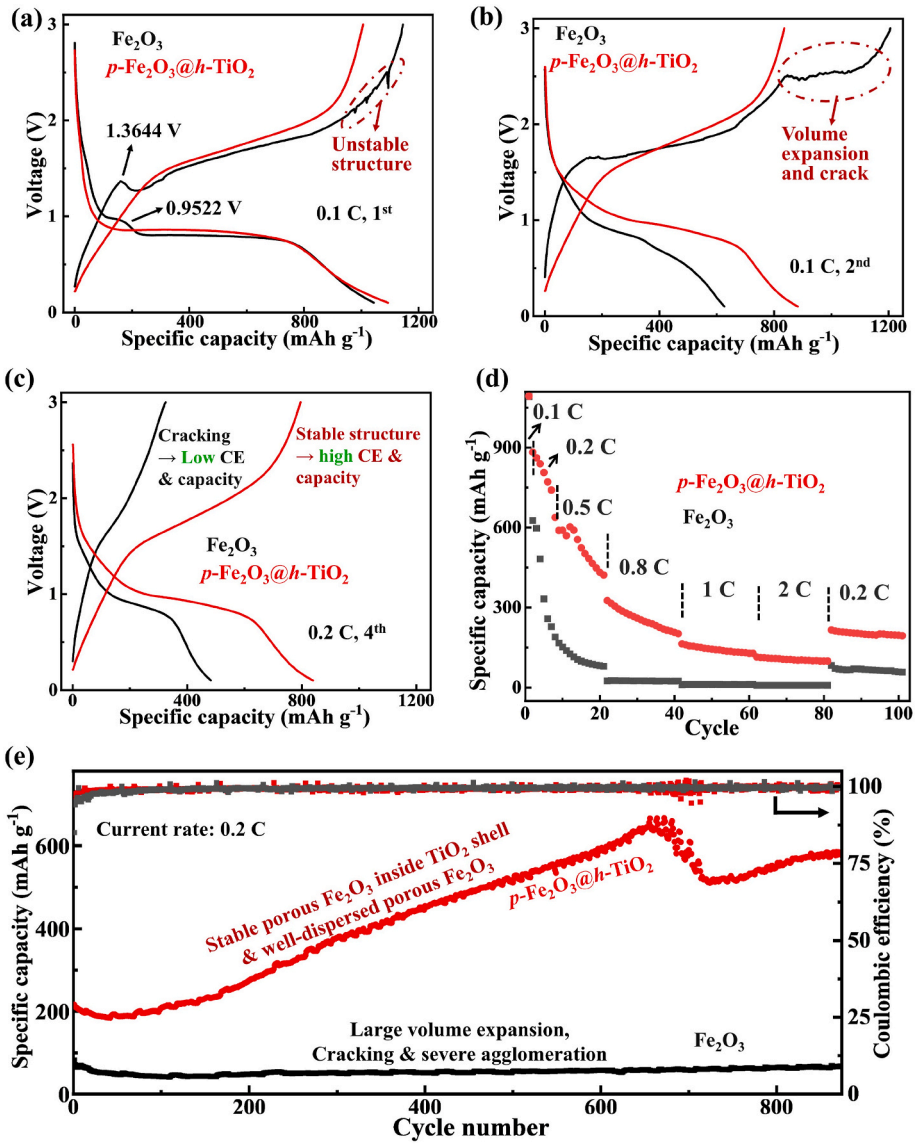

Fig. 5. Cycling performance of the commercial Fe_2O_3 and *p*-Fe_2O_3@*h*-TiO_2 electrodes in half cells. Discharge/charge profiles for the (a) 1st, (b) 2nd and (c) 4th cycles at 0.1 C and 0.2 C, respectively. (d) Rate performance at 0.1, 0.2, 0.5, 0.8, 1 and 2 C. (e) Cycling performance at 0.2 C (1 C = 1007 mA g^{-1}).

displayed in Fig. 5d, the commercial Fe_2O_3 has a rapid capacity decay when the current density increases from 0.1 C (1043.8 mAh g^{-1}) to 0.2 C (167–626.8 mAh g^{-1}), which is due to the sluggish Li ion diffusion among agglomerated Fe_2O_3 particles. In contrast, *p*-Fe_2O_3@*h*-TiO_2 builds high specific capacities of 1093.4 mAh g^{-1} and 740.5–882.7 mAh g^{-1} at 0.1 C and 0.2 C, respectively. Moreover, at 0.5 C, 0.8 C, 1 C and 2 C, the specific capacities of *p*-Fe_2O_3@*h*-TiO_2 are ~502.4 mAh g^{-1}, ~247.8 mAh g^{-1}, ~141.1 mAh g^{-1} and ~102.4 mAh g^{-1}, respectively, while that of the commercial Fe_2O_3 are ~105.2 mAh g^{-1}, ~24.7 mAh g^{-1}, ~11.3 mAh g^{-1} and ~8.1 mAh g^{-1}, respectively. When the current density decreases to 0.2 C again, the capacity of *p*-Fe_2O_3@*h*-TiO_2 and the commercial Fe_2O_3 increases to 201.4 mAh g^{-1} and 67 mAh g^{-1}, respectively. This significantly improved rate capacity of *p*-Fe_2O_3@*h*-TiO_2 demonstrates its excellent Li-ion diffusion kinetics.

The long cycling performance was tested at a current density of 0.2 C. The evolution of specific capacities and their corresponding Coulombic efficiencies are shown in Fig. 5e. It is found the capacity of the commercial Fe_2O_3 keeps at a very low value of ~41 mAh g^{-1}. In sharp contrast, the capacity of *p*-Fe_2O_3@*h*-TiO_2 increases from 215.8 mAh g^{-1} at the first cycle to 641.3 mAh g^{-1} at the 666th cycle. The capacity increase is a common phenomenon for transition metal oxide anodes, which can be ascribed to (1) the kinetic activation, (2) the enhanced interfacial lithium storage caused by the growth of SEI, and/or (3) the involvement of more inner active materials in electrochemical reactions after long cycles [49–51]. In the 666th-722nd cycles, due to some structure changes, the capacity of *p*-Fe_2O_3@*h*-TiO_2 decreases to 516.3 mAh g^{-1} at the 722nd cycle, and thereafter, slightly increases to 585.1 mAh g^{-1} at the 874th cycle.

3.6. Characterization of cycled *p*-Fe_2O_3@*h*-TiO_2 electrodes

The morphology of the uncycled and cycled electrodes of the commercial Fe_2O_3 and *p*-Fe_2O_3@*h*-TiO_2 after 3 cycles was observed to study the improved electrochemical performance. For the uncycled electrodes (Fig. S6a, S6b, S7a, S7b), no specific difference can be found between the commercial Fe_2O_3 and *p*-Fe_2O_3@*h*-TiO_2. Regarding the cycled commercial Fe_2O_3 electrode, a rough surface can be found and large agglomerated particles are observed on the electrode (Fig. 6a, S6c). This result demonstrates the severe agglomeration of Fe_2O_3 particles during cycling processes, which induces unstable electrode structure and poor ionic/electronic conductivity among active materials (Fig. 6b). On the contrary, the cycled *p*-Fe_2O_3@*h*-TiO_2 electrode shows a homogenous

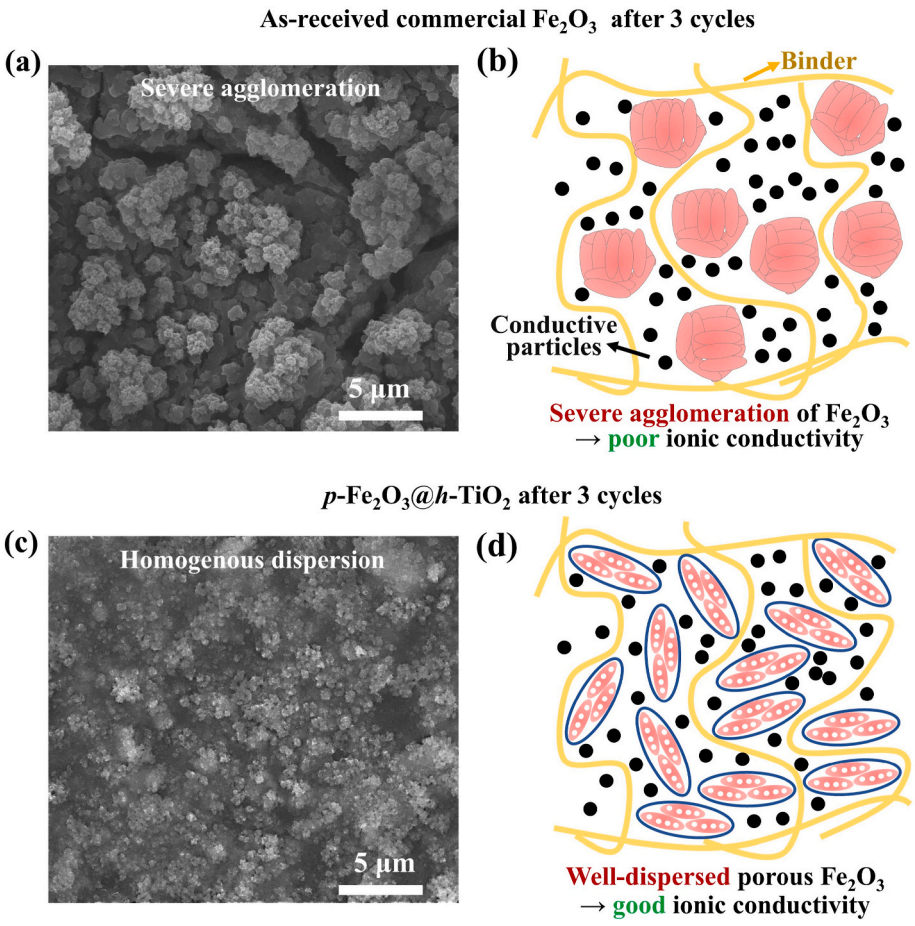

Fig. 6. Morphology of (a) cycled commercial Fe_2O_3 and (c) p-Fe_2O_3@h-TiO_2 electrodes after 3 cycles. Morphology evolution schematics of (b) Fe_2O_3 and (d) p-Fe_2O_3@h-TiO_2 electrodes.

morphology, and the particles have a good dispersion after cycling process (Fig. 6c, S6d). It is confirmed that the TiO_2 shell effectively prevents the agglomeration of Fe_2O_3 and stabilizes the electrode structure of p-Fe_2O_3@h-TiO_2 (Fig. 6d), improving the ionic/electronic conductivities, and thus, leading to excellent cycling performance.

4. Conclusions

In conclusion, through a viable, "green" fabrication process with a high yield, we fabricate a hollow structure with a TiO_2 shell encapsulating the porous Fe_2O_3 (p-Fe_2O_3@h-TiO_2) from as-received commercial Fe_2O_3 particles (for cosmetic applications). The synthesis processes only include glucose as an "etching" agent and simple heating procedures without the involvement of any organic solvents or hard-controllable environments. Specifically, glucose and Fe_2O_3 concentrations are optimized to effectively form a desirable hollow structure in high yields. Characterizations of the nanostructures, chemical compositions, crystallizations and thermal behaviors for the intermediate/final products demonstrate the successful synthesis of p-Fe_2O_3@h-TiO_2. The TiO_2 shell effectively accommodates the volume change, decreases the pulverization, and lessens the agglomeration of the Fe_2O_3 particles. Meanwhile, the porous Fe_2O_3 core facilitates Li diffusion, decreasing the impedance of batteries. As a result, the p-Fe_2O_3@h-TiO_2 anode displays an excellent capacity of 664 mAh g^{-1} (vs. 58.7 mAh g^{-1} of the commercial Fe_2O_3) after 650 cycles at 0.2 C. This work provides an attractive "green" and efficient fabrication method of converting commercial abundant resources such as Fe_2O_3 into effective electrode materials of energy storage systems.

Author contributions

Chenxu Wang: Writing-original manuscript, Experimental design, Investigation, Conceptualization, and Formal analysis. Pedaballi Sireesha: Writing-review & editing. Jing Shang: Raman & XRD testing, Review. John McCloy: Writing-review & editing, Supervision. Jin Liu: Writing - review & editing, Supervision, Funding acquisition. Wei-Hong Zhong: Writing - review & editing, Supervision, Funding acquisition.

Declaration of competing interest

The authors declare that they have no known competing financial interests or personal relationships that could have appeared to influence the work reported in this paper.

Acknowledgements

This work was supported by NSF CBET 1929236, United states. The authors would like to gratefully acknowledge the support on microscopy characterizations from the Franceschi Microscopy & Imaging Center at Washington State University, United states. We thank Dr. Qiang Zhang and Mr. Sheng Yu for the BET test.

Appendix A. Supplementary data

Supplementary data to this article can be found online at https://doi.org/10.1016/j.ceramint.2023.07.234.

References

[1] M. Li, J. Lu, Z. Chen, K. Amine, 30 Years of lithium-ion batteries, Adv. Mater. 30 (2018) 1–24, https://doi.org/10.1002/adma.201800561.
[2] H. Cheng, J.G. Shapter, Y. Li, G. Gao, Recent progress of advanced anode materials of lithium-ion batteries, J. Energy Chem. 57 (2021) 451–468, https://doi.org/10.1016/J.JECHEM.2020.08.056.
[3] M. Gao, P. Zhou, P. Wang, J. Wang, C. Liang, J. Zhang, Y. Liu, FeO/C anode materials of high capacity and cycle stability for lithium-ion batteries synthesized by carbothermal reduction, J. Alloys Compd. 565 (2013) 97–103, https://doi.org/10.1016/j.jallcom.2013.03.012.
[4] S. Fang, D. Bresser, S. Passerini, Transition metal oxide anodes for electrochemical energy storage in lithium- and sodium-ion batteries, in: Transit. Met. Oxides Electrochem. Energy Storage, John Wiley & Sons, Ltd, 2022, pp. 55–99, https://doi.org/10.1002/9783527817252.ch4.
[5] C. Wang, W. Zhong, Promising sustainable technology for energy storage devices : natural protein-derived active materials, Electrochim. Acta 441 (2023), 141860, https://doi.org/10.1016/j.electacta.2023.141860.
[6] W. Zhang, Y. Xu, H. Li, C. Wang, B. Qin, Z. Li, Y. Chen, K. Jiang, H. Zhang, Incorporating SnO2 nanodots into wood flour-derived hierarchically porous carbon as low-cost anodes for superior lithium storage, J. Electroanal. Chem. 856 (2020), 113654, https://doi.org/10.1016/j.jelechem.2019.113654.
[7] Y. Wang, Y. Xu, J. Zhou, C. Wang, W. Zhang, Z. Li, F. Guo, H. Chen, H. Zhang, Highly dispersed SnO2 nanoparticles confined on xylem fiber-derived carbon frameworks as anodes for lithium-ion batteries, J. Electroanal. Chem. 879 (2020), 114753, https://doi.org/10.1016/j.jelechem.2020.114753.
[8] C. Wang, X. Yang, M. Zheng, Y. Xu, Synthesis of β-FeOOH nanorods adhered to pine-biomass carbon as a low-cost anode material for Li-ion batteries, J. Alloys Compd. 794 (2019) 569–575, https://doi.org/10.1016/j.jallcom.2019.04.074.
[9] M.V. Reddy, T. Yu, C.H. Sow, Z.X. Shen, C.T. Lim, G.V.S. Rao, B.V.R. Chowdari, α-Fe2O3 nanoflakes as an anode material for li-ion batteries, Adv. Funct. Mater. 17 (2007) 2792–2799, https://doi.org/10.1002/adfm.200601186.
[10] M. Golmohammad, A. Sazvar, M. Maleki Shahraki, F. Golestanifard, Synthesis and characterization of bar-like maghemite (γ-Fe2O3) as an anode for Li-ion batteries, Ceram. Int. 48 (2022) 27148–27153, https://doi.org/10.1016/J.CERAMINT.2022.06.026.
[11] Y. Li, Y. Huang, Y. Zheng, R. Huang, J. Yao, Facile and efficient synthesis of A-Fe2O3 nanocrystals by glucose-assisted thermal decomposition method and its application in lithium ion batteries, J. Power Sources 416 (2019) 62–71, https://doi.org/10.1016/j.jpowsour.2019.01.080.
[12] C. Wang, M. Zheng, Y. Xu, D. Wang, D. Liu, Cu ion induced morphology change of hematite microspheres as lithium ion battery anode material by solvothermal synthesis, Ceram. Int. 45 (2019) 2940–2947, https://doi.org/10.1016/j.ceramint.2018.09.222.
[13] D. Wu, Y. Niu, C. Wang, H. Wu, Q. Li, Z. Chen, B. Xu, H. Li, L.Y. Zhang, γ-Fe2O3 nanoparticles stabilized by holey reduced graphene oxide as a composite anode for lithium-ion batteries, J. Colloid Interface Sci. 552 (2019) 633–638, https://doi.org/10.1016/J.JCIS.2019.05.091.
[14] J.M. Jeong, B.G. Choi, S.C. Lee, K.G. Lee, S.J. Chang, Y.K. Han, Y.B. Lee, H.U. Lee, S. Kwon, G. Lee, C.S. Lee, Y.S. Huh, Hierarchical hollow spheres of Fe2O3@polyaniline for lithium ion battery anodes, Adv. Mater. 25 (2013) 6250–6255, https://doi.org/10.1002/adma.201302710.
[15] J.S. Chen, T. Zhu, X.H. Yang, H.G. Yang, X.W. Lou, Top-down fabrication of α-Fe2O3 single-crystal nanodiscs and microparticles with tunable porosity for largely improved lithium storage properties, J. Am. Chem. Soc. 132 (2010) 13162–13164, https://doi.org/10.1021/JA1060438/SUPPL_FILE/JA1060438_SI_001.PDF.
[16] F. Zhu, H. Shi, Z. Yu, C. Wang, W. Cheng, X. Zhou, F. Yang, Y. Zhang, X. Zhang, Acid-etched Fe/Fe2O3nanoparticles encapsulated into carbon cloth as a novel voltammetric sensor for the simultaneous detection of Cd2+and Pb2, Analyst 146 (2021) 691–697, https://doi.org/10.1039/d0an01861a.
[17] P. Li, X. Yan, Z. He, J. Ji, J. Hu, G. Li, K. Lian, W. Zhang, α-Fe2O3 concave and hollow nanocrystals: top-down etching synthesis and their comparative photocatalytic activities, CrystEngComm 18 (2016) 1752–1759, https://doi.org/10.1039/c5ce02097b.
[18] J. Lin, A.R.O. Raji, K. Nan, Z. Peng, Z. Yan, E.L.G. Samuel, D. Natelson, J.M. Tour, Iron oxide nanoparticle and graphene nanoribbon composite as an anode material for high-performance li-ion batteries, Adv. Funct. Mater. 24 (2014) 2044–2048, https://doi.org/10.1002/adfm.201303023.
[19] F. Han, D. Li, W.C. Li, C. Lei, Q. Sun, A.H. Lu, Nanoengineered polypyrrole-coated Fe2O3@C multifunctional composites with an improved cycle stability as lithium-ion anodes, Adv. Funct. Mater. 23 (2013) 1692–1700, https://doi.org/10.1002/adfm.201202254.
[20] Q.Q. Xiong, J.P. Tu, X.H. Xia, X.Y. Zhao, C.D. Gu, X.L. Wang, A three-dimensional hierarchical Fe2O3@NiO core/shell nanorod array on carbon cloth: a new class of anode for high-performance lithium-ion batteries, Nanoscale 5 (2013) 7906–7912, https://doi.org/10.1039/c3nr02258g.
[21] X. Zhang, H. Chen, Y. Xie, J. Guo, Ultralong life lithium-ion battery anode with superior high-rate capability and excellent cyclic stability from mesoporous Fe2O3@TiO2 core-shell nanorods, J. Mater. Chem. A. 2 (2014) 3912–3918, https://doi.org/10.1039/c3ta14317a.
[22] F. Li, G. Luo, J. Yu, W. Huang, D. Xu, W. Chen, X. Huang, S. Yang, Y. Fang, X. Yu, Terminal hollowed Fe2O3@SnO2 heterojunction nanorods anode materials with enhanced performance for lithium-ion battery, J. Alloys Compd. 773 (2019) 778–787, https://doi.org/10.1016/j.jallcom.2018.09.159.
[23] S. Li, J. Niu, Y.C. Zhao, K.P. So, C. Wang, C.A. Wang, J. Li, High-rate aluminium yolk-shell nanoparticle anode for Li-ion battery with long cycle life and ultrahigh capacity, Nat. Commun. 6 (2015) 1–7, https://doi.org/10.1038/ncomms8872.
[24] S. Fang, L. Shen, G. Xu, P. Nie, J. Wang, H. Dou, X. Zhang, Shan Fang, Laifa Shen, Guiyin Xu, Ping Nie, Jie Wang, Hui Dou, and Xiaogang Zhang, ACS Appl. Mater. Interfaces 6 (2014) 6497–6503.
[25] Q. Tian, Z. Zhang, L. Yang, S.I. Hirano, Encapsulation of SnO2 nanoparticles into hollow TiO2 nanowires as high performance anode materials for lithium ion batteries, J. Power Sources 253 (2014) 9–16, https://doi.org/10.1016/j.jpowsour.2013.12.049.
[26] J. Wang, X. Luo, C. Young, J. Kim, Y.V. Kaneti, J. You, Y.M. Kang, Y. Yamauchi, K. C.W. Wu, A glucose-assisted hydrothermal reaction for Directly transforming metal-organic frameworks into hollow carbonaceous materials, Chem. Mater. 30 (2018) 4401–4408, https://doi.org/10.1021/acs.chemmater.8b01792.
[27] S. hua Luo, D. bei Hu, H. Liu, J. zhe Li, T.F. Yi, Hydrothermal synthesis and characterization of A-Fe2O3/C using acid-pickled iron oxide red for Li-ion batteries, J. Hazard Mater. 368 (2019) 714–721, https://doi.org/10.1016/j.jhazmat.2019.01.106.
[28] H. Shibata, H. Mihara, T. Mukai, T. Ogura, H. Kohno, T. Ohkubo, H. Sakai, M. Abe, Preparation and formation mechanism of mesoporous titania particles having crystalline wall, Chem. Mater. 18 (2006) 2256–2260, https://doi.org/10.1021/cm0524042.
[29] L. Zhang, H. Bin Wu, X.W. Lou, Iron-oxide-based advanced anode materials for lithium-ion batteries, Adv. Energy Mater. 4 (2014), 1300958, https://doi.org/10.1002/aenm.201300958.
[30] D. Cao, H. Li, L. Pan, J. Li, X. Wang, P. Jing, X. Cheng, W. Wang, J. Wang, Q. Liu, High saturation magnetization of γ 3-Fe2 O3 nano-particles by a facile one-step synthesis approach, Sci. Rep. 6 (2016) 1–9, https://doi.org/10.1038/srep32360.
[31] B. Moongraksathum, P.T. Hsu, Y.W. Chen, Photocatalytic activity of ascorbic acid-modified TiO2 sol prepared by the peroxo sol–gel method, J. Sol. Gel Sci. Technol. 78 (2016) 647–659, https://doi.org/10.1007/s10971-016-3993-4.
[32] M. Farahmandjou, F. Soflaee, Synthesis and characterization of α-Fe2O3 nanoparticles by simple co-precipitation method, Phys. Chem. Res. 3 (2015) 191–196, https://doi.org/10.22036/pcr.2015.9193.
[33] R.G. Morais, N. Rey-Raap, R.S. Costa, C. Pereira, A. Guedes, J.L. Figueiredo, M.F. R. Pereira, Hydrothermal carbon/carbon nanotube composites as electrocatalysts for the oxygen reduction reaction, J. Compos. Sci. 4 (2020) 6–8, https://doi.org/10.3390/jcs4010020.
[34] P. Praveen, G. Viruthagiri, S. Mugundan, N. Shanmugam, Structural, optical and morphological analyses of pristine titanium di-oxide nanoparticles - synthesized via sol-gel route, Spectrochim. Acta Part A Mol. Biomol. Spectrosc. 117 (2014) 622–629, https://doi.org/10.1016/j.saa.2013.09.037.
[35] N. Husnain, E. Wang, S. Fareed, M.T. Anwar, Comparision on the low-temperature NH3-SCR performance of γ-Fe2O3 catalysts prepared by two different methods, Catalysts 9 (2019), https://doi.org/10.3390/catal9121018.
[36] K. Thamaphat, P. Limsuwan, B. Ngotawornchai, Phase characterization of TiO 2 powder by XRD and TEM, Kasetsart J./Nat. Sci. 42 (2008) 357–361.
[37] S. Sahoo, K. Agarwal, A. Singh, B. Polke, K. Raha, Characterization of γ- and α-Fe2O3 nano powders synthesized by emulsion precipitation-calcination route and rheological behaviour of α-Fe2O3, Int. J. Eng. Sci. Technol. 2 (2011) 118–126, https://doi.org/10.4314/ijest.v2i8.63841.
[38] P. Kumar, H. No-Lee, R. Kumar, Synthesis of phase pure iron oxide polymorphs thin films and their enhanced magnetic properties, J. Mater. Sci. Mater. Electron. 25 (2014) 4553–4561, https://doi.org/10.1007/s10854-014-2203-9.
[39] I. Chourpa, L. Douziech-Eyrolles, L. Ngaboni-Okassa, J.F. Fouquenet, S. Cohen-Jonathan, M. Soucé, H. Marchais, P. Dubois, Molecular composition of iron oxide nanoparticles, precursors for magnetic drug targeting, as characterized by confocal Raman microspectroscopy, Analyst 130 (2005) 1395–1403, https://doi.org/10.1039/b419004a.
[40] S. Challagulla, K. Tarafder, R. Ganesan, S. Roy, Structure sensitive photocatalytic reduction of nitroarenes over TiO2, Sci. Rep. 7 (2017) 1–11, https://doi.org/10.1038/s41598-017-08599-2.
[41] B. Kumar, M.S. Reddy, K.D. Dwivedi, A. Dahiya, J.N. Babu, L.R. Chowhan, Synthesis of in situ immobilized iron oxide nanoparticles (Fe3O4) on microcrystalline cellulose: ecofriendly and recyclable catalyst for Michael addition, Appl. Organomet. Chem. 36 (2022) 1–10, https://doi.org/10.1002/aoc.6455.
[42] C. Miao, T. Shi, G. Xu, S. Ji, C. Ye, Photocurrent enhancement for Ti-doped Fe2O3 thin film photoanodes by an in situ solid-state reaction method, ACS Appl. Mater. Interfaces 5 (2013) 1310–1316, https://doi.org/10.1021/am302575p.
[43] G. Dai, L. Zhan, C. Guan, M. Huang, Optimization of molding process parameters for CF/PEEK composites based on Taguchi method, Compos. Adv. Mater. 30 (2021), 263498332110018, https://doi.org/10.1177/26349833211001882.
[44] W. Choi, H.C. Shin, J.M. Kim, J.Y. Choi, W.S. Yoon, Modeling and applications of electrochemical impedance spectroscopy (Eis) for lithium-ion batteries, J. Electrochem. Sci. Technol. 11 (2020) 1–13, https://doi.org/10.33961/jecst.2019.00528.
[45] C. Wang, C. Ying, J. Shang, S.E. Karcher, J. McCloy, J. Liu, W.H. Zhong, A bioinspired coating for stabilizing Li metal batteries, ACS Appl. Mater. Interfaces 14 (2022) 43886–43896, https://doi.org/10.1021/acsami.2c10667.
[46] N. Yan, X. Zhou, Y. Li, F. Wang, H. Zhong, H. Wang, Q. Chen, Fe2 O3 nanoparticles wrapped in multi-walled carbon nanotubes with enhanced lithium storage capability, Sci. Rep. 3 (2013) 1–6, https://doi.org/10.1038/srep03392.
[47] J. Chen, E. Wang, J. Mu, B. Ai, T. Zhang, W. Ge, L. Zhang, CNTs–C@TiO2 composites with 3D networks as anode material for lithium/sodium ion batteries, J. Mater. Sci. 54 (2019) 592–604, https://doi.org/10.1007/s10853-018-2814-2.

[48] S. Wei, D. Di Lecce, R. Messini D'Agostini, J. Hassoun, Synthesis of a high-capacity α-Fe2O3@C conversion anode and a high-voltage LiNi0.5Mn1.5O4Spinel cathode and their combination in a Li-ion battery, ACS Appl. Energy Mater. 4 (2021) 8340–8349, https://doi.org/10.1021/acsaem.1c01585.

[49] H. Kim, W. Choi, J. Yoon, J.H. Um, W. Lee, J. Kim, J. Cabana, W.S. Yoon, Exploring anomalous charge storage in anode materials for next-generation Li rechargeable batteries, Chem. Rev. 120 (2020) 6934–6976, https://doi.org/10.1021/acs.chemrev.9b00618.

[50] Y. Zheng, Y. Li, J. Yao, Y. Huang, S. Xiao, Facile synthesis of porous tubular NiO with considerable pseudocapacitance as high capacity and long life anode for lithium-ion batteries, Ceram. Int. 44 (2018) 2568–2577, https://doi.org/10.1016/j.ceramint.2017.11.017.

[51] M.F. Hassan, Z. Guo, Z. Chen, H. Liu, α-Fe2O3 as an anode material with capacity rise and high rate capability for lithium-ion batteries, Mater. Res. Bull. 46 (2011) 858–864, https://doi.org/10.1016/j.materresbull.2011.02.011.